



Published in final edited form as:

ACS Appl Mater Interfaces. 2018 August 22; 10(33): 27621–27630. doi:10.1021/acsami.8b08005.

Erythrocyte-Derived Theranostic Nanoplatfoms for Near Infrared Fluorescence Imaging and Photodestruction of Tumors

Joshua M. Burns[†], Raviraj Vankayala[†], Jenny T. Mac[‡], and Bahman Anvari^{*†‡}

[†]Department of Bioengineering, University of California, Riverside, 900 University Avenue, Riverside, California 92521, United States

[‡]Department of Biochemistry, University of California, Riverside, 900 University Avenue, Riverside, California 92521, United States

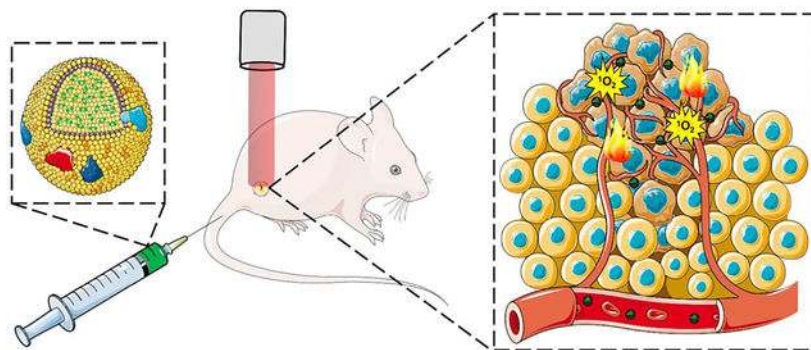
Abstract

Nanoparticles activated by near-infrared (NIR) excitation provide a capability for optical imaging and photodestruction of tumors. We have engineered optical nanoconstructs derived from erythrocytes, which are doped with the FDA-approved NIR dye, indocyanine green (ICG). We refer to these constructs as NIR erythrocyte-mimicking transducers (NETs). Herein, we investigate the phototheranostic capabilities of NETs for fluorescence imaging and photodestruction of SKBR3 breast cancer cells and subcutaneous xenograft tumors in mice. Our cellular studies demonstrate that NETs are internalized by these cancer cells and localized to their lysosomes. As evidenced by NIR fluorescence imaging and in vivo laser irradiation studies, NETs remain available within tumors at 24 h postintravenous injection. In response to continuous wave 808 nm laser irradiation at intensity of 680 mW/cm² for 10–15 min, NETs mediate the destruction of cancer cells and tumors in mice through synergistic photochemical and photothermal effects. We demonstrate that NETs are effective in mediating photoactivation of Caspase-3 to induce tumor apoptosis. Our results provide support for the effectiveness of NETs as theranostic agents for fluorescence imaging and photodestruction of tumors and their role in photoinduced apoptosis initiated by their localization to lysosomes.

Graphical Abstract

*Corresponding Author: anvarib@ucr.edu.

The authors declare the following competing financial interest(s): R.V. and B.A. have a financial interest in Radoptics LLC, which is pursuing the commercial development of the nanoparticles reported in this manuscript. This interest did not interfere with the scientific work and judgment and the objectivity of these investigators in regards to experimental procedures, data analyses and reporting, interpretation of results, and any other aspect of the study.



Keywords

apoptosis; lysosomes; indocyanine green; red blood cells; photodynamic therapy; photothermal therapy

INTRODUCTION

Light-activated materials present a potential theranostic platform for image-guided phototherapy.^{1–3} In particular, use of near-infrared (NIR) wavelengths (≈ 750 – 1450 nm) is especially advantageous since relatively deep (≈ 2 – 3 cm) optical imaging and phototherapy can be achieved due to reduced light absorption and scattering by endogenous constituents. To date, indocyanine green (ICG) remains as the only NIR-activated agent approved by FDA for specific clinical applications including ophthalmic angiography, car-diocirculatory measurements, assessment of hepatic function, and blood flow evaluation.^{4,5} ICG has also been investigated for potential applications ranging from sentinel lymph node mapping in patients with different types of cancer to imaging intracranial aneurysm and cerebral arteriovenous malformations.^{6–11}

In addition to its optical imaging capabilities, ICG has also been investigated as a photosensitizer for photodynamic therapy of choroidal melanomas and breast adenocarcinomas,^{12,13} as well as a photothermal agent for treatment of port wine stains.¹⁴ However, ICG's major drawbacks are its short plasma half-life (≈ 3 – 5 min) and nonspecific interactions with various biological macromolecules, particularly serum albumin and high density lipoproteins. To overcome these limitations, ICG has been encapsulated within various constructs, including micelles, liposomes, silica, and synthetic polymers.^{15–20}

Use of mammalian cells such as erythrocytes, lymphocytes, and macrophages, or constructs derived from them, are receiving increased attention as delivery platforms due to increased circulation time and biocompatibility.^{21–25} For example, Hu et al. reported that nanoconstructs (≈ 80 nm diameter) composed of a poly(lactic-co-glycolic acid) (PLGA) core coated with erythrocyte-derived membranes were retained in blood for 3 days with circulation half-life of ≈ 8 h in mice.²⁶ Piao et al. have reported that the circulation half-life of gold nanocages cloaked with erythrocyte membranes (≈ 90 nm diameter) was ≈ 9.5 h.²⁴ Rao et al. did not observe systemic toxicity 15 days after intravenous injection of erythrocyte membrane-coated upconversion nanoparticles in mice.²³

We previously provided the first report on the engineering of nanosized vesicles derived from erythrocytes loaded with ICG and their utility for fluorescence imaging and photodestruction of human dermal microvascular endothelial cells. We refer to these constructs as NIR erythrocyte-mimicking transducers (NETs) since once activated by NIR light, they can transduce the absorbed photons energy to generate heat, emit fluorescence, or mediate production of reactive oxygen species (ROS). Herein, we investigate the phototheranostic capabilities of NETs for near-infrared fluorescence imaging and photodestruction of cancer cells and subcutaneous xenograft tumors in mice. We demonstrate that NETs remain available within tumors at 24 h postintravenous injection and mediate the destruction of cancer cells' and tumors through synergistic photochemical and photothermal effects in response to continuous wave laser irradiation. We report for the first time that NETs are localized to cancer cells lysosomes and upon photoexcitation can induce Caspase-3 activation, leading to tumor apoptosis.

RESULTS AND DISCUSSION

Characterization of NETs.

The mean peak hydrodynamic diameter of NETs as estimated by dynamic light scattering (DLS) was ≈ 79 nm (Figure 1a). We used log-normal fits to estimate the mean \pm standard deviation (SD) diameter of NETs as 85 ± 1 nm. We have previously published transmission electron²⁷ and scanning electron²⁸ microscopic images of NETs and demonstrated that DLS-based measurements of NETs' diameters are consistent with those made by electron microscopy. The polydispersity index (PDI) value for this set of NETs was 0.2, meaning that the standard deviation in diameter is 20% of the mean value. Nanoparticles with PDI values in the range of 0.1–0.4 are considered as moderately polydispersed.²⁹ Since the hydrodynamic diameters of NETs are <200 nm, they are likely to be effective for extravasation into tumors through the enhanced permeability and retention effect, induced by the leaky tumor vasculature and impaired lymphatic drainage.^{30,31}

The absorption spectra of free $13 \mu\text{M}$ ICG dissolved in ≈ 310 mOsm phosphate buffer saline (PBS) (defined as the $1\times$ PBS) and NETs fabricated using 1.1 mM ICG in the loading buffer are shown in Figure 1b. The free ICG equivalent concentration loaded into these NETs [ICG_{NETs}] was estimated as $\approx 10 \mu\text{M}$ (see Experimental Section). The absorption spectrum of free ICG exhibited primary and secondary peaks at 698 and 776 nm, associated with the H-like aggregate and monomeric forms of ICG, respectively.³² In contrast, NET suspended in $1\times$ PBS, showed a dominant spectral peak at 804 nm, suggesting that the monomeric ICG was the dominant form within these NETs. The bathochromic (red) spectral shift in the monomeric absorption of free ICG from 776 to 804 nm in NETs is consistent with our previous results.^{27,28,33} This shift can be attributed to the binding of ICG molecules to phospholipids and membrane proteins of the NETs, causing a change in the molecular energy levels of ICG, as well as the local solvent environment surrounding ICG within the NETs.^{32,34}

In response to photoexcitation at 720 ± 2.5 nm, the normalized fluorescence emission spectra ($\chi(\lambda)$) (see eq 1) of $4 \mu\text{M}$ free ICG and NETs ($[\text{ICG}_{\text{NETs}}] \approx 2 \mu\text{M}$) showed respective peaks at 792 and 796 nm, associated with the monomer form, respectively (Figure

1c). The normalized fluorescence emission spectra had a similar bathochromic shift from 792 nm (associated with the monomer form of free ICG) to 796 nm (associated with emission from the monomeric form of ICG in NETs). The peak value of $\chi(\lambda)$ for NETs was $\approx 15\%$ higher than that of free ICG. This increase may be due to reduced self-aggregation of ICG as a result of its binding to proteins and lipids in the membrane shell of NETs. Similar fluorescent enhancement has been reported for ICG binding to lipids,¹⁷ proteins in fetal bovine serum,³² and albumin.³⁵

Photostability and NETs-Mediated Singlet Oxygen Generation.

To gain insight on photostability of ICG in both free and nanoencapsulated formulations, we acquired their respective absorption spectra immediately after being laser irradiated at 808 nm with incident intensity (I_0) of 680 mW/cm² for up to 15 min (Figure 2a). We prepared solutions of free ICG (22 μ M) and NETs ($[ICG_{NETs}] \approx 18 \mu$ M) in 1 \times PBS so that the absorbance values for both free ICG and NETs at 808 nm were 1.8. With increasing laser irradiation times, there were corresponding reductions in the absorption spectra (Figure 2a). These reductions can be attributed to photoinduced chemical modification of ICG molecules to produce a leuco form of the dye with converted sp² to sp³ carbon hybridization and/or induce cleavage of the π -conjugation along the polyene segment of the dye while keeping the aromatic benzindotricarbocyanine moieties intact.²⁷ At 808 nm, free ICG had the lowest percentage decrease in its absorbance values as compared with NETs (Figure 2b). For example, after 15 min of irradiation, the 808 nm absorbance values of free ICG and NETs irradiated at 680 mW/cm² decreased by 26.2% and 60.0%, respectively. Greater reductions in 808 nm absorbance values of NETs upon laser irradiation may be due to induced molecular conformational changes in ICG as a result of nanoencapsulation.

We used 1,3-diphenylisobenzofuran (DPBF) as a probe to assess the generation of singlet oxygen (¹O₂) in response to 808 nm photoexcitation of free ICG and NETs (see Experimental Section). Laser irradiation of DPBF dissolved in dimethylformamide (DMF) at $I_0 = 680 \text{ mW/cm}^2$ for up to 80 s did not alter the absorbance value at 411 nm (Figure 2c), confirming that there was no photoinduced production of ¹O₂ in the absence of NIR absorbing molecules or particles. However, in the presence of free ICG or NETs, the normalized DPBF absorbance at 411 nm progressively decreased with increased 808 nm laser irradiation time (Figure 2c). Generation of ¹O₂ is consistent with the type II photochemistry where the intersystem crossing of ICG (in free or nanoencapsulated form) to the excited triplet state is followed by energy transfer to the ground state molecular oxygen, producing ¹O₂.

Fluorescence Imaging of SKBR3 Breast Cancer Cells Incubated with NETs.

SKBR3 human breast cancer cells were incubated at 37°C with PBS (negative control), 44 μ M free ICG (positive control), or NETs ($[ICG_{NETs}] \approx 36 \mu$ M) for 3 h. Following incubation, cells were washed and then fluorescently imaged. While there was no or minimal NIR fluorescence emission from SKBR3 cells incubated with PBS or free ICG, NETs-incubated cells emitted NIR fluorescence (Figure 3a).

Flow cytometry results confirmed that the mean fluorescence intensity of cells incubated with NETs were significantly higher than those associated with cells incubated with free ICG or PBS ($n = 3$, $p < 0.01$) (Figure 3b). These results further validate that NETs were effectively uptaken by the cells, whereas most of free ICG was removed as a result of washing the cells. These results demonstrate that NETs serve as an effective platform to deliver their cargo (ICG) to cancer cells.

To determine the cellular localization of NETs, we used 4',6-diamidino-2-phenylindole (DAPI) and LysoTracker, fluorescent probes that respectively stain the nucleus and lysosomes, and imaged the cells by laser scanning confocal fluorescence microscopy (LSCFM) (Figure 3c). LysoTracker and ICG fluorescence from NETs spatially overlapped, suggesting that NETs were localized to lysosomes of the cells and positioned at the periphery of the nucleus. Our analysis of the images indicated Pearson's value of $R = 0.99$, confirming that the intensity distributions were highly correlated. Similarly, Costes' P value of 1.00 confirmed the colocalization of the intensities from each pixel. Although not investigated here, it is possible that NETs may also accumulate in mitochondria. For example, it has been demonstrated that an analog form of ICG, consisting of a cyclohexenyl substitution in the middle of the polymethine linker and two asymmetrical amphipathic N-alkyl side chains, accumulated in the mitochondria of MCF-7 and 4T1 breast cancer cells.³⁶ In another study, localization of magnetic complex nanoparticles loaded with ICG to the mitochondria of A549 adenocarcinomic alveolar basal epithelial cell line was reported.³⁷

Laser Irradiation of SKBR3 Breast Cancer Cells Incubated with NETs.

SKBR3 cells were incubated at 37°C with PBS (negative control), 176 μM free ICG (positive control), or NETs ($[\text{ICG}_{\text{NETs}}] \approx 144 \mu\text{M}$) for 3 h. Following incubation, cells were washed and then irradiated at 808 nm for 15 min using $I_0 = 680 \text{ mW/cm}^2$. We evaluated the viability of the cells following laser irradiation. Cells were stained with Calcein acetoxymethyl (AM) and ethidium homodimer-1 (EthD-1) to fluorescently visualize the live and dead cells, respectively (Figure 4a). In response to laser irradiation, $\approx 93\%$ of ICG-treated SKBR3 cells remained viable. However, only 32% of NETs-treated cells were viable after laser irradiation at these parameters (Figure 4b).

We also evaluated the effects of $[\text{ICG}_{\text{NETs}}]$ on photodestruction of SKBR3 cells. The fraction of cell death progressively increased as $[\text{ICG}_{\text{NETs}}]$ increased (Figure 4c). With increased $[\text{ICG}_{\text{NETs}}]$ from 18 to 144 μM , the fractions of cell death increased from 23% to 68% for SKBR3 cells incubated with NETs.

To investigate if ROS production was a contributing mechanism to photoinduced destruction of SKBR3 cells, we used the molecular 2,7-dichlorofluorescein diacetate (DCFH-DA) (see Experimental Section). Cells incubated with NETs showed dichlorofluorescein (DCF) fluorescence whereas the incubation of cells with PBS or ICG did not result in any noticeable DCF fluorescence emission (Figure 5a). These results indicate that NETs were uptaken by SKBR3 cancer cells and mediated ROS production in response to laser irradiation.

To determine if ROS included $^1\text{O}_2$ as a constituent, we used sodium azide as an $^1\text{O}_2$ quencher (see Experimental Section).³⁸ Upon pretreatment with sodium azide, the DCF fluorescence emission from SKBR3 cells incubated with NETs was quenched after laser irradiation, indicating the DCF emission from cells not treated with sodium azide was associated with $^1\text{O}_2$ production in response to laser irradiation. Collectively, our in vitro results based on analysis of cell viability (Figure 4) and the use of molecular probes for ROS detection (Figure 5) support the presence of a photochemical mechanism in destruction of cancer cells incubated with NETs and laserirradiated at 808 nm using $I_0 = 680 \text{ mW/cm}^2$ for 15 min.

NIR Fluorescence Imaging and Laser Irradiation of Tumors.

We investigated the efficacy of NETs in NIR fluorescence imaging of tumors. Tumors were extracted 24 h after tail vein injection of PBS (control) or NETs ($[\text{ICG}_{\text{NETs}}] \approx 980 \mu\text{M}$) and were immediately imaged by NIR photoexcitation and collecting the fluorescence emission. NETs offered the capability to image the tumor (Figure 6a), indicating that they were present within the tumor at 24 h postinjection. These results show that encapsulation of ICG within erythrocyte-derived nanovesicles provided an effective method to prolong the circulation of ICG, making it available for an intended application (e.g., tumor imaging) for at least 24 h.

We assessed the capability of NETs in mediating photo-destruction of xenograft tumors implanted subcutaneously in mice. Laser irradiation was done 24 h after intravenous injection of NETs via the tail vein. To investigate if there was a photothermal effect during laser irradiation, we recorded the in vivo temperature changes using a thermocouple needle probe inserted at $\approx 1 \text{ mm}$ below the skin and $\approx 2 \text{ mm}$ outside of the laser-irradiated spot. Laser irradiation at $I_0 = 680 \text{ mW/cm}^2$ resulted in a temperature rise of $\approx 11^\circ\text{C}$ at the end of the 10 min of irradiation time (Figure 6b). This temperature rise underestimates the actual temperature distributions within the tumor and is a measure of the heat diffusion from the irradiated tumor site. Nevertheless, these measurements suggest that there was a photothermal effect during laser irradiation.

To investigate the presence of cellular apoptosis in response to laser irradiation, some of the tumors were extracted immediately after laser irradiation and imaged by fluorescent immunostaining to detect the presence of Caspase-3. As evidenced by fluorescence emission, there was Caspase-3 activation in mice injected with NETs and irradiated at 680 mW/cm^2 for 10 min (Figure 6c). Analysis of these images confirmed that NETs were effective in mediating photoinduced activation of Caspase-3 as evidenced by statistically significant higher values of fluorescence intensity associated with Caspase-3 (Figure 6d). Results of in vivo laser irradiation of tumors provide further evidence that NETs remained in circulation for at least 24 h.

In response to laser irradiation at $I_0 = 680 \text{ mW/cm}^2$ in conjunction with NETs, we observed reductions in tumor volumes as early as 2 days postlaser irradiation (Figure 6e). By 10 days postirradiation, tumor volumes were nearly zero. In contrast, laser irradiation in the absence of NETs was associated with growths in tumor volumes, indicating the effectiveness of NETs in mediating photodestruction of tumors.

Some important aspects of this study were the findings that (1) NETs were localized to lysosomes as evidenced by LSCFM results (Figure 3) and (2) NETs mediated photoactivation of Caspase-3 in tumors (Figure 6c,d). These results indicate that lysosomal localization of NETs with subsequent laser irradiation, at the indicated parameters, can induce cellular apoptosis. Photoinduced damage to lysosomes membranes leads to release of cathepsin proteases and other hydrolytic enzymes into the cytosol³⁹ to activate apoptosis mediator proteins.⁴⁰ Pro-apoptotic mediators include a subgroup of the B-cell lymphoma 2 (BCL-2) family of proteins.⁴¹ Bid is a member of the BCL-2 subgroup containing only the BH3 domain, which is cleaved by proteases to truncated Bid (tBid).⁴² Upon translocation to the outer membranes of mitochondria, tBid can directly promote mitochondrial outer membrane permeabilization (MOMP)^{43,44} or play a role in recruitment of cytosolic Bax, another member of the proapoptotic BCL-2 group, to mediate MOMP,^{45,46} leading to release of pro-apoptotic proteins including cytochrome c.^{47,48} The release of cytochrome c as a signal will finally activate the executors including Caspase-3 for cell death.⁴⁰ Therefore, our findings are consistent with photoinduced lysosomal damage as the basis to induce apoptosis. Nevertheless, on the basis of the observed temperature increases (Figure 6b), photothermal effects could have also contributed to the destruction of cancer cells (Figure 4) and tumors (Figure 6e).

Various light-activated nanoparticle systems are under investigation in relation to cancer imaging and therapy. On the basis of material type, such systems can generally be classified into semiconductors (e.g., quantum dots (QDs)), metallic (e.g., gold, silver) and organic (i.e., carbon nanomaterials such as graphene and fullerene) particles.^{49,50} There are certain attractive features with these types of materials such as photostability of QDs, tunable optical properties of QDs and gold nanomaterials, light-induced local surface plasmon resonance effects, and quantum confinement effects due to nanosize (<10 nm) of carbon materials that result in their distinct optical properties. Limitations of these materials include cytotoxicity associated with certain constituents of QDs, potential oxidative stress and genotoxicity associated with gold nanoparticles,⁵¹ safety concerns with carbon nanotubes,⁵² and short vascular retention time of carbon nanomaterials due to their excretion through the kidneys, which stems from their small size (<10 nm).

In comparison to these light-activated nanoparticle systems, the major key advantages of NETs stem from its constituent materials and composition that lead to the distinct properties and capabilities of these particles: (1) As constructs that can be engineered autologously (or from similar blood types), NETs are potentially nonimmunogenic, nontoxic, and biocompatible. (2) CD47 is a key membrane glycoprotein expressed in erythrocytes,⁵³ which impedes phagocytosis. Our previous results²⁸ indicate that CD47 remains on the surface of NETs, suggesting that NETs may remain shielded from the immune system and have extended retention time within the vasculature, hence providing their cargo (e.g., ICG) available for delivery to the tumor site over a longer time. Herein, as evidenced by NIR fluorescence imaging and in vivo laser irradiation studies, NETs remain available within tumors at 24 h postintravenous injection. In comparison, the reported halfives of ICG encapsulated in PLGA or liposomal nanoparticles following intravenous injection are, respectively, on the order of approximately 5 min and less than a minute in blood.^{19,54} (3) Fabrication of NETs is simple. Particles can be produced within about a day at room

temperature and pressure without any complex chemical synthesis procedures and use of specialized and expensive equipment.

Our results are consistent with the findings by Ren et al. in which nanoparticles (≈ 150 nm diameter) comprised of an ICG-bound albumin and perfluorocarbon core encapsulated by an erythrocyte-derived membrane shell were used as phototherapeutic agents.⁵⁵ These investigators also reported that both photothermal and photochemical effects (i.e., production of singlet oxygen) can serve as the basis for destruction of xenograft tumors in mice in response to 808 nm laser irradiation at $I_0 = 1 \text{ W/cm}^2$ for 3 min.

A synergistic effect of photothermal and photochemical mechanisms indicates that the photophysics of ICG allows for both vibrational relaxations from its excited electronic states as well as intersystem crossing to a triplet state under the irradiation parameters investigated in this study to ultimately lead to photodestruction of tumors. The photophysical properties of ICG can be exploited to endow NETs with capabilities for fluorescence imaging and therapeutic effects. In this context, NETs can serve as platforms for light-activated theranostics as applied to a variety of solid tumors. For example, a particularly important clinical application is in relation to ovarian cancer theranostics. Patients with ovarian cancer are most often diagnosed with late stage disease with metastasis to the peritoneum. One of the most important prognostic factors is the degree of cytoreduction at surgery. However, small tumor nodules (< 1 mm) are difficult to detect by current preoperative imaging methods or visually during surgery. Furthermore, tumors may reside along critical structures to be removed without inducing significant morbidity. Surgical procedures such as diaphragm stripping, splenectomy, distal pancreatectomy, liver resection, or cholecystectomy may be required to remove such intraperitoneal tumors. NETs can potentially be used as lightactivated theranostic nanoprobe during intraoperative procedures to enable visualization of small tumor nodules for surgical removal or mediate photodestruction of inoperable tumors.

CONCLUSIONS

We have demonstrated the phototheranostic capabilities of NETs for fluorescence imaging and photodestruction of cancer cells and subcutaneous xenograft tumors in mice. NETs are internalized by cancer cells and localized to the lysosomes. NETs remain available within tumors at 24 h postintravenous injection and mediate the destruction of cancer cells and xenograft tumors through synergistic photochemical and photothermal effects at the irradiation parameters investigated. Our results indicate that NETs are capable of mediating photoinduced tumor destruction initiated by their localization to lysosomes with subsequent activation of Caspase-3 and culminated in tumor apoptosis.

EXPERIMENTAL SECTION

Fabrication of NETs.

Erythrocytes were separated from bovine whole blood (Rockland Immunochemicals, Inc., Limerick, PA) by centrifugation (5 min, 1300g, 4°C). The supernatant, containing the plasma and buffy coat, was discarded, and the resulting packed erythrocytes were washed

twice with 1× (310 mOsm, pH ~ 8.0) phosphate buffer saline (PBS). Packed erythrocytes were then subjected to sequential hypotonic treatment with 0.5× PBS (155 mOsm, pH ~ 8.0) and 0.25× PBS (77.5 mOsm, pH ~ 8.0), respectively. The centrifugation process (20 000g, 15 min, 4°C) was repeated until all the hemoglobin was depleted, resulting in opaque white pellet containing micron-sized hemoglobin-depleted erythrocyte ghosts (EGs).

To obtain nanosized EGs, the micron-sized EGs were extruded 10 times through 800 nm polycarbonate porous membranes (Nuclepore Track-Etched Membranes, Whatman, Florham Park, New York), followed by 10 more extrusions through 400 nm polycarbonate membranes and another 10 times through 200 nm polycarbonate membranes using an extruder (LIPEX Extruder, TRANSFERRA Nanosciences Inc., Burnaby, Canada). To concentrate the nanosized EGs, 10 mL of nanosized EGs was centrifuged (99 000g, 1 h, 4°C) and resuspended in 1 mL of 1× PBS.

To load ICG into nanosized EGs, 1 mL of nanosized EGs solution, concentrated by 10 times, was incubated with 3 mL of ICG dissolved in water (at concentration of 2 mg/mL) and 3 mL of hypotonic buffer ($\text{Na}_2\text{HPO}_4/\text{Na}_2\text{H}_2\text{PO}_4$, 140 mOsm, pH ~ 5.8), resulting in 6 mg of ICG in 7 mL of the loading buffer. The corresponding concentration of ICG in this loading buffer was ~1.1 mM (considering the molecular weight of ICG as ~775 Da). The suspension was incubated for 5 min at 4°C in the dark, centrifuged at 74 000g for 30 min, and then washed three times using 1× PBS to remove any non-encapsulated ICG. The pellet containing ICG-encapsulated EGs (i.e., NETs) was removed and resuspended in 1 mL of 1× PBS (4°C). To avoid saturation in measurements of NIR absorbance values during absorption spectral recordings, this solution of NETs was further diluted by a factor of 80 using 1× PBS. We then acquired the absorption spectrum of the 1:80 diluted solution of NETs.

Next, we proceeded to estimate the free ICG equivalent concentration within the population of NETs $[\text{ICG}_{\text{NETs}}]$ as follows. We first acquired the absorption spectra of ICG dissolved in water at concentrations in the range of 2–10 μM . We chose water as the solvent since the absorption spectra of NETs resembles that of ICG dissolved in water at concentrations less than ~20 μM . The spectra were then spectrally integrated in the range of 600–900 nm, and the resulting values (A_{int}) were plotted against ICG concentrations to obtain a calibration curve ($R^2 = 0.99$). We then used the value of A_{int} associated with the 1:80 diluted solution of NETs in conjunction with the calibration curve to estimate $[\text{ICG}_{\text{NETs}}] \approx 12.25 \mu\text{M}$. Finally, we estimated $[\text{ICG}_{\text{NETs}}]$ for the undiluted NETs to be ~980 μM as the product of 12.25 μM and the dilution factor of 80. In a similar fashion, we prepared various dilutions of the NETs solution with values of $[\text{ICG}_{\text{NETs}}] \approx 2, 10, 18, 36, 72, \text{ and } 144 \mu\text{M}$.

Characterization of NETs.

The hydrodynamic diameters of NETs suspended in 1× PBS were measured by dynamic light scattering (DLS) (Zetasizer NanoZS90, Malvern Instruments Ltd., Malvern, United Kingdom). The absorption spectra of NETs ($[\text{ICG}_{\text{NETs}}] \approx 10 \mu\text{M}$) and 13 μM free ICG suspended in 1× PBS were obtained using a UV–visible spectrophotometer (Cary 50 UV–vis spectrophotometer, Agilent Technologies, Santa Clara, CA) with optical path length of 1 cm. The fluorescence emission spectra of NETs ($[\text{ICG}_{\text{NETs}}] \approx 2 \mu\text{M}$) and 4 μM free ICG

were acquired in response to 720 ± 2.5 nm and recorded using a fluorimeter (Fluorolog-3 spectrofluorometer, Edison, NJ). We normalized the fluorescence emission spectra ($\chi(\lambda)$) as

$$\chi(\lambda) = \frac{F(\lambda)}{\left(1 - 10^{-A(\lambda_{\text{ex}})}\right)} \quad (1)$$

where A and F are the wavelength (λ) dependent absorbance and intensity of the emitted fluorescence light, respectively, and λ_{ex} is the excitation wavelength.

Photostability of NETs.

NETs suspended in PBS ($[\text{ICG}_{\text{NETs}}] \approx 18 \mu\text{M}$) and $22 \mu\text{M}$ of ICG dissolved in PBS were prepared. Samples were then laser-irradiated at 808 nm using an intensity (I_0) value of 680 mW/cm^2 (9 mm diameter focal spot) for durations (t_{laser}) ranging between 1 and 15 min. Immediately following each experiment at a given t_{laser} , we acquired the absorption spectra of the samples and normalized them to the absorbance value at 808 nm ($A(\lambda = 808 \text{ nm})$) prior to laser irradiation (defined as time t_0).

Detection of Singlet Oxygen Generation.

We used $10 \mu\text{M}$ 1,3-diphenylisobenzofuran (DPBF) as a probe to detect the generation of singlet oxygen ($^1\text{O}_2$) in response to 808 nm photoexcitation of $11 \mu\text{M}$ free ICG or NETs ($[\text{ICG}_{\text{NETs}}] \approx 18 \mu\text{M}$). DPBF has an absorption peak at 411 nm in dissolved in dimethylformamide (DMF).⁵⁶ Upon reacting with $^1\text{O}_2$, DPBF undergoes 1,4-cycloaddition to form an endoperoxide product, resulting in decreased 411 nm absorption. Samples were irradiated at $I_0 = 680 \text{ mW/cm}^2$ for 10 s. An aliquot of sample was then withdrawn, and the absorbance at 411 nm was recorded using a UV-visible spectrophotometer. The absorbance value at 411 nm was normalized to the absorbance value at 411 nm prior to laser irradiation. In the negative control experiment, DPBF solution without NETs or free ICG was irradiated at $I_0 = 680 \text{ mW/cm}^2$, and the 411 nm absorbance values were determined and normalized as above.

Cell Culture.

SKBR3 human breast cancer cells (ATCC, Manassas, VA) were cultured in Rosewell Park Memorial Institute (RPMI) 1640 medium (Mediatech Inc., Manassas, VA) supplemented with 10% fetal bovine serum (FBS) and 1% penicillin/streptomycin (Corning Inc., Corning, NY) at 37°C in 5% humidified CO_2 . Cells were used for in vitro experiments and implanted in mice to induce tumors.

Assessment of NETs Uptake by SKBR3 Cancer Cells.

We used bright-field and NIR fluorescence imaging, flow cytometry, and laser scanning confocal fluorescence microscopy (LSCFM) to evaluate the uptake of NETs by SKBR3 cancer cells. Cells were cultured in 96-well plates for NIR fluorescence imaging and 12-well plates for flow cytometry. For LSCFM, cells were grown on poly L-lysine coated coverslips in 12-well plates. After 24 h, cells were incubated in RPMI medium containing PBS

(negative control), NETs ($[ICG_{NETs}] \approx 36 \mu\text{M}$), or $44 \mu\text{M}$ free ICG (positive control) for 3 h. Cells were then washed three times with PBS prior to imaging or flow cytometry.

NIR fluorescence emission ($>770 \text{ nm}$) in response to $740 \pm 35 \text{ nm}$ excitation by a Nikon Mercury/Xenon arc lamp was captured by an electron multiplier gained charge-coupled device (EM-CCD) camera (Quant EM-CCD, C9100–14 Hamamatsu, Shizuoka-ken, Japan). The camera exposure time was set at 0.7 s for NIR fluorescence emission and 0.03 s for bright-field images and gain of 1.0. We present falsely colored microscopic images with NIR fluorescent emission due to ICG (red channel) merged with bright-field (gray channel).

For flow cytometry experiments, the RPMI medium was removed, and cells were incubated with trypsin for 5 min. After incubation, fresh RPMI was added to halt trypsinization, and cells were subsequently centrifuged at 125g for 5 min. The supernatant was removed, and the pellet was then resuspended in $1\times$ PBS. A flow cytometer (BD FACSAria cell sorter, San Jose, CA) with photoexcitation at 633 nm and emission collection at $>785 \text{ nm}$ was used to measure the NIR signals from cells that had been incubated with PBS, NETs, or free ICG. All studies were done using three different samples. During flow cytometry, a minimum of $\approx 10\,000$ events were counted for each triplicate within the gating region.

For LSCFM experiments, the RPMI medium was removed after incubating the cells with NETs, and cells were then incubated with LysoTracker HCK-123 (Invitrogen, Carlsbad, CA) for 2 h. Immediately after staining with LysoTracker, we fixed and permeated the cells using 4% paraformaldehyde and 2% Tween 20, respectively. We then mounted the slide with ProLong Gold Antifade containing 4',6-diamidino-2-phenylindole (DAPI) (Invitrogen, Carlsbad, CA) and used a confocal microscope (Leica SP5, Leica Microsystems Inc., Buffalo Grove, IL) with photoexcitation at 405, 488, and 633 nm, corresponding to DAPI, LysoTracker, and ICG absorption, respectively. Fluorescence emission was collected at 420–480, 500–610, and $>655 \text{ nm}$, respectively. We present falsely colored microscopic images corresponding to DAPI (blue channel), LysoTracker emission (green channel), and ICG NIR emission (red channel). For colocalization analysis, we used ImageJ to calculate the pixel intensity correlation using the two methods, Pearson and Costes.⁵⁷

Laser Irradiation of SKBR3 Cancer Cells.

To investigate the photodestructive capability of NETs, SKBR3 cells were cultured in a 96-well plate. After 24 h, cells were incubated with RPMI medium containing PBS, free ICG (44 and $176 \mu\text{M}$), or NETs (with specific value of $[ICG_{NETs}] = 18, 36, 72, \text{ or } 144 \mu\text{M}$) for 3 h in the dark at 37°C . After incubation, cells were then washed three times with PBS and fresh medium was added. We subsequently irradiated the cells at 808 nm using I_0 values of 680 mW/cm^2 for 15 min.

To assess the viability of cells following laser irradiation, cells were incubated in RPMI medium containing $2 \mu\text{M}$ Calcein acetoxymethyl (AM) and $4 \mu\text{M}$ ethidium homodimer-1 (EthD-1) (ThermoFisher Scientific, Waltham, MA) as the respective live/dead assays for 30 min. Cells were then washed with PBS and fluorescently imaged in response to Calcein AM excitation at $485 \pm 35 \text{ nm}$ and EthD-1 excitation at $543 \pm 22 \text{ nm}$ by a Nikon Mercury/Xenon arc lamp. Respective fluorescence emission over the spectral bands of 524 ± 24 and 593

± 40 nm were captured by an EM-CCD camera with exposure time set at 0.03 s. We present falsely colored microscopic images with Calcein AM fluorescent emission (green channel) overlaid with EthD-1 fluorescence emission (red channel). Cell viability in each well was calculated using a fluorescent microplate reader (Molecular Devices FlexStation II 384, Harlow Scientific).

To detect the presence of ROS in response to NIR laser irradiation of SKBR3 cancer cells, we used the molecular probe 2',7'-dichlorofluorescein diacetate (DCFH-DA) (Sigma-Aldrich, St. Louis, MO). Once the nonfluorescent DCFH-DA is oxidized by ROS, it is converted into a fluorescent molecule 2',7'-dichlorofluorescein (DCF).⁵⁸ In a subset of experiments, cells treated with PBS, 18 μ M NETs, and 22 μ M free ICG for 3 h (as described above) were further incubated with 25 μ M DCFH-DA in RPMI medium for 30 min prior to laser irradiation at the parameters indicated above. Following irradiation, we imaged the cells in bright-field and fluorescence modes. The DCF fluorescence emission (524 ± 24 nm) in response to 485 ± 35 nm excitation by a Nikon Mercury/Xenon arc lamp was captured by an EM-CCD camera. The camera exposure time was set at 0.2 s for DCF fluorescence emission and 0.03 s for bright-field images and gain of 1.0. We present falsely colored microscopic images with DCF fluorescent emission (green channel) merged with bright-field (gray channel).

To determine if ROS included singlet oxygen ($^1\text{O}_2$) as a constituent, we used sodium azide as a $^1\text{O}_2$ quencher probe.³⁸ In a subset of experiments, we pretreated the SKBR3 cells with DCFH-DA (as described above), washed them after 30 min, and then incubated them in RPMI medium containing 50 mM sodium azide for 45 min prior to laser irradiation at the indicated parameters above.

Animal Study.

Female Nu/J mice (20–25 g; 6–8 weeks) were purchased from Jackson Laboratory (Bar Harbor, Maine) and utilized in this study under a protocol approved by the University of California, Riverside Institutional Animal Care and Use Committee (A-20140022). We injected $\approx 1 \times 10^7$ SKBR3 cancer subcutaneously into the thighs. Mice were monitored until the tumor sizes reached approximately 15 mm³. The tumor volume was calculated as $D \times d^2/2$, where D and d were the larger and smaller diameter of each tumor.

Tumor-bearing mice were randomly divided into three groups with four animals in each group. Group 1 received PBS injection without laser irradiation. Group 2 received PBS injection and 808 nm laser irradiation using $I_0 = 680$ mW/cm² for 10 min. Group 3 received NETs [ICG_{NETs} ≈ 980 μ M] injection and 808 nm laser irradiation using $I_0 = 680$ mW/cm² for 10 min. We administered 100 μ L of PBS or NETs intravenously via tail vein injection while the animal was anesthetized. Laser irradiation was performed at 24 h postinjection of PBS or NETs with a beam diameter of 9 mm. We measured the temperature change in response to laser irradiation by inserting a mini-hypodermic thermocouple (0.2 mm thermocouple diameter) (HYP0, OMEGA, Norwalk, CT) connected to a LabQuest data acquisition system (Vernier, Beaverton, OR) ≈ 1 mm below the skin and about 2 mm outside the laser-irradiated spot. Following the experimental procedures, animals were allowed to recover. We assessed the efficacy of NETs in mediating photoinduced reductions in tumor

size by measuring the tumor volumes following each treatment at every 2 day interval and for up to 16 days after laser irradiation. We estimated the relative tumor volumes (V/V_0) during this time interval by dividing the volume of each tumor (V) on the measurement day by the initial tumor volume (V_0) on the day of laser irradiation. Animals were subsequently euthanized on day 16 following laser irradiation.

In a subset of experiments, an animal from each group was euthanized immediately after laser irradiation. Tumors were removed and frozen at -80°C for later analysis. Approximately 7 days later, tumors were thawed and sectioned in $10\ \mu\text{m}$ thicknesses using a cryostat microtome (CM1950 cryostat, Buffalo Grove, Illinois) and stained with fluorescein isothiocyanate (FITC)-labeled Caspase-3 antibody (BD Biosciences, San Jose, CA) as an established method to assay for cell apoptosis.^{59–61} Fluorescent emission ($524 \pm 24\ \text{nm}$) in response to $485 \pm 35\ \text{nm}$ excitation by a Nikon Mercury/Xenon arc lamp was captured by an EM-CCD camera with exposure time set at 0.2 s. Mean and SDs of the image intensities ($n = 5$ images) were quantified using ImageJ.

To evaluate the feasibility of NETs in tumor imaging, in a subset of experiments, $100\ \mu\text{L}$ of PBS or NETs [$\text{ICG}_{\text{NETs}} \approx 980\ \mu\text{M}$] was administered by tail vein injection. At 24 h postinjection, animals were euthanized, and tumors were extracted. Extracted tumors were fluorescently imaged in a dark box. Two light emitting diodes delivering $700 \pm 30\ \text{nm}$ excitation light were used for illumination. Fluorescence emission was captured using a CCD camera (Pixis 1024B, Roper Scientific, Trenton, NJ) equipped with a long pass filter transmitting wavelengths greater than $810\ \text{nm}$. To prevent pixel saturation, the camera exposure time was set to 90 s.

ACKNOWLEDGMENTS

This study was supported in parts by grants from the National Science Foundation (CBET-1509218), National Cancer Institute at National Institutes of Health (R43-CA210715-A1), University of California Cancer Research Coordinating Committee (5-44189-34912), and University of California, Riverside Office of Research & Economic Development.

REFERENCES

- (1). Kim H; Chung K; Lee S; Kim DH; Lee H Near-Infrared Light-Responsive Nanomaterials for Cancer Theranostics. Wiley Interdiscip. Rev.: Nanomed. Nanobiotechnol 2016, 8, 23–45. [PubMed: 25903643]
- (2). Shan G; Weissleder R; Hilderbrand SA Upconverting Organic Dye Doped Core-Shell Nano-Composites for Dual-Modality NIR Imaging and Photo-Thermal Therapy. Theranostics 2013, 3, 267–274. [PubMed: 23606913]
- (3). Lee M-Y; Lee C; Jung HS; Jeon M; Kim KS; Yun SH; Kim C; Hahn SK Biodegradable Photonic Melanoidin for Theranostic Applications. ACS Nano 2016, 10, 822–831. [PubMed: 26623481]
- (4). Frangioni JV In Vivo Near-Infrared Fluorescence Imaging. Curr. Opin. Chem. Biol 2003, 7, 626–634. [PubMed: 14580568]
- (5). Marshall MV; Rasmussen JC; Tan I-C; Aldrich MB; Adams KE; Wang X; Fife CE; Maus EA; Smith LA; Sevcik-Muraca EM Near-Infrared Fluorescence Imaging in Humans with Indocyanine Green: A Review and Update. Open Surg. Oncol. J 2010, 2, 12–25. [PubMed: 22924087]
- (6). Roessler K; Krawagna M; Dorfler A; Buchfelder M; Ganslandt O Essentials in Intraoperative Indocyanine Green Videoangiography Assessment for Intracranial Aneurysm Surgery:

Conclusions from 295 Consecutively Clipped Aneurysms and Review of the Literature. *Neurosurg. Focus* 2014, 36, E7 (pp 7).

- (7). Crane LMA; Themelis G; Arts HJG; Buddingh KT; Brouwers AH; Ntziachristos V; van Dam GM; van der Zee AGJ Intraoperative Near-Infrared Fluorescence Imaging for Sentinel Lymph Node Detection in Vulvar Cancer: First Clinical Results. *Gynecol. Oncol* 2011, 120, 291–295. [PubMed: 21056907]
- (8). Hirche C; Murawa D; Mohr Z; Kneif S; Hunerbein M ICG Fluorescence-Guided Sentinel Node Biopsy for Axillary Nodal Staging in Breast Cancer. *Breast Cancer Res. Treat* 2010, 121, 373–378. [PubMed: 20140704]
- (9). Sevick-Muraca EM; Sharma R; Rasmussen JC; Marshall MV; Wendt JA; Pham HQ; Bonefas E; Houston JP; Sampath L; Adams KE; Blanchard DK; Fisher RE; Chiang SB; Elledge R; Mawad ME Imaging of Lymph Flow in Breast Cancer Patients after Microdose Administration of a Near-Infrared Fluorophore: Feasibility Study. *Radiology* 2008, 246, 734–741. [PubMed: 18223125]
- (10). Verbeek FPR; Troyan SL; Mieog JSD; Liefers G-J; Moffitt LA; Rosenberg M; Hirshfield-Bartek J; Gioux S; van de Velde CJH; Vahrmeijer AL; Frangioni JV Near-Infrared Fluorescence Sentinel Lymph Node Mapping in Breast Cancer: A Multicenter Experience. *Breast Cancer Res. Treat* 2014, 143, 333–342. [PubMed: 24337507]
- (11). Zaidi HA; Abila AA; Nakaji P; Chowdhry SA; Albuquerque FC; Spetzler RF Indocyanine Green Angiography in the Surgical Management of Cerebral Arteriovenous Malformations: Lessons Learned in 130 Consecutive Cases. *Neurosurgery* 2014, 10 (2), 246–251. [PubMed: 24535264]
- (12). Liggett PE; Lavaque AJ; Chaudhry NA; Jablon EP; Quiroz-Mercado H Preliminary Results of Combined Simultaneous Transpupillary Thermotherapy and ICG-Based Photodynamic Therapy for Choroidal Melanoma. *Ophthalm. Surg. Lasers Imaging* 2005, 36, 463–470.
- (13). Montazerabadi AR; Sazgarnia A; Bahreyni-Toosi MH; Ahmadi A; Aledavood A The Effects of Combined Treatment with Ionizing Radiation and Indocyanine Green-Mediated Photodynamic Therapy on Breast Cancer Cells. *J. Photochem. Photobiol., B* 2012, 109, 42–49. [PubMed: 22325306]
- (14). Klein A; Baumler H; Buschmann M; Landthaler M; Babilas P A Randomized Controlled Trial to Optimize Indocyanine Green-Augmented Diode Laser Therapy of Capillary Malformations. *Lasers Surg. Med* 2013, 45, 216–224. [PubMed: 23619901]
- (15). Kirchherr AK; Briel A; Mäder K Stabilization of Indocyanine Green by Encapsulation within Micellar Systems. *Mol. Pharmaceutics* 2009, 6, 480–491.
- (16). Wu L; Fang S; Shi S; Deng J; Liu B; Cai L Hybrid Polypeptide Micelles Loading Indocyanine Green for Tumor Imaging and Photothermal Effect Study. *Biomacromolecules* 2013, 14, 3027–3033. [PubMed: 23941524]
- (17). Kraft JC; Ho RJ Interactions of Indocyanine Green and Lipid in Enhancing Near-Infrared Fluorescence Properties: The Basis for Near-Infrared Imaging in Vivo. *Biochemistry* 2014, 53, 1275–1283. [PubMed: 24512123]
- (18). Bahmani B; Gupta S; Upadhyayula S; Vullev VI; Anvari B Effect of Polyethylene Glycol Coatings on Uptake of Indocyanine Green Loaded Nanocapsules by Human Spleen Macrophages in Vitro. *J. Biomed. Opt* 2011, 16, 051303 (pp 10). [PubMed: 21639563]
- (19). Saxena V; Sadoqi M; Shao J Polymeric Nanoparticulate Delivery System for Indocyanine Green: Biodistribution in Healthy Mice. *Int. J. Pharm. (Amsterdam, Neth.)* 2006, 308, 200–204.
- (20). Sharma P; Bengtsson NE; Walter GA; Sohn H-B; Zhou G; Iwakuma N; Zeng H; Grobmyer SR; Scott EW; Moudgil BM Gadolinium-Doped Silica Nanoparticles Encapsulating Indocyanine Green for Near Infrared and Magnetic Resonance Imaging. *Small* 2012, 8, 2856–2868. [PubMed: 22744832]
- (21). Yoo J-W; Irvine DJ; Discher DE; Mitragotri S Bio-Inspired, Bioengineered and Biomimetic Drug Delivery Carriers. *Nat. Rev. Drug Discovery* 2011, 10, 521–535. [PubMed: 21720407]
- (22). Muzykantov VR Drug Delivery by Red Blood Cells: Vascular Carriers Designed by Mother Nature. *Expert Opin. Drug Delivery* 2010, 7, 403–427.
- (23). Rao L; Meng Q-F; Bu L-L; Cai B; Huang Q; Sun ZJ; Zhang WF; Li A; Guo S-S; Liu W; Wang T-H; Zhao X-Z Erythrocyte Membrane-Coated Upconversion Nanoparticles with Minimal

Protein Adsorption for Enhanced Tumor Imaging. *ACS Appl. Mater. Interfaces* 2017, 9, 2159–2168. [PubMed: 28050902]

- (24). Piao JG; Wang L; Gao F; You YZ; Xiong Y; Yang L Erythrocyte Membrane Is an Alternative Coating to Polyethylene Glycol for Prolonging the Circulation Lifetime of Gold Nanocages for Photothermal Therapy. *ACS Nano* 2014, 8, 10414–10425. [PubMed: 25286086]
- (25). Peng J; Yang Q; Li WT; Tan LW; Xiao Y; Chen L; Hao Y; Qian Z Erythrocyte-Membrane-Coated Prussian Blue/Manganese Dioxide Nanoparticles as H₂O₂-Responsive Oxygen Generators to Enhance Cancer Chemotherapy/Photothermal Therapy. *ACS Appl. Mater. Interfaces* 2017, 9, 44410–44422. [PubMed: 29210279]
- (26). Hu C-MJ; Zhang L; Aryal S; Cheung C; Fang RH; Zhang L Erythrocyte Membrane-Camouflaged Polymeric Nanoparticles as a Biomimetic Delivery Platform. *Proc. Natl. Acad. Sci. U. S. A* 2011, 108, 10980–10985. [PubMed: 21690347]
- (27). Bahmani B; Bacon D; Anvari B Erythrocyte-Derived PhotoTheranostic Agents: Hybrid Nano-Vesicles Containing Indocyanine Green for Near Infrared Imaging and Therapeutic Applications. *Sci. Rep* 2013, 3, 2180 (pp 7). [PubMed: 23846447]
- (28). Mac JT; Nuñez V; Burns JM; Guerrero YA; Vullev VI; Anvari B Erythrocyte-Derived Nano-Probes Functionalized with Antibodies for Targeted Near Infrared Fluorescence Imaging of Cancer Cells. *Biomed. Opt. Express* 2016, 7, 1311–1322. [PubMed: 27446657]
- (29). Nobbmann U; Morfesis A Light Scattering and Nanoparticles. *Mater. Today* 2009, 12, 52–54.
- (30). Nakamura H; Jun F; Maeda H Development of Next-Generation Macromolecular Drugs Based on the EPR Effect: Challenges and Pitfalls. *Expert Opin. Drug Delivery* 2015, 12, 53–64.
- (31). Torchilin V Tumor Delivery of Macromolecular Drugs Based on the EPR Effect. *Adv. Drug Delivery Rev* 2011, 63, 131–135.
- (32). Jung B; Vullev VI; Anvari B Revisiting Indocyanine Green: Effects of Serum and Physiological Temperature on Absorption and Fluorescence Characteristics. *IEEE J. Sel. Top. Quantum Electron* 2014, 20, 149–157.
- (33). Burns JM; Saager R; Majaron B; Jia W; Anvari B Optical Properties of Biomimetic Probes Engineered from Erythrocytes. *Nanotechnology* 2017, 28, 035101 (pp 12). [PubMed: 27966473]
- (34). Sibrian-Vazquez M; Escobedo JO; Lowry M; Fronczek FR; Strongin RM Field Effects Induce Bathochromic Shifts in Xanthene Dyes. *J. Am. Chem. Soc* 2012, 134, 10502–10508. [PubMed: 22642754]
- (35). Philip R; Penzkofer A; Baumler W; Szeimies RM; Abels C Absorption and Fluorescence Spectroscopic Investigation of Indocyanine Green. *J. Photochem. Photobiol., A* 1996, 96, 137–148.
- (36). Tan X; Luo S; Long L; Wang Y; Wang D; Fang S; Ouyang Q; Su Y; Cheng T; Shi C Structure-Guided Design and Synthesis of a Mitochondria-Targeting Near-Infrared Fluorophore with Multimodal Therapeutic Activities. *Adv. Mater* 2017, 29, 1704196 (pp 9).
- (37). Guo R; Peng H; Tian Y; Shen S; Yang W Mitochondria-Targeting Magnetic Composite Nanoparticles for Enhanced Phototherapy of Cancer. *Small* 2016, 12, 4541–4552. [PubMed: 27390093]
- (38). Li MY; Cline CS; Koker EB; Carmichael HH; Chignell CF; Bilski P Quenching of Singlet Molecular Oxygen (¹O₂) by Azide Anion in Solvent Mixtures. *Photochem. Photobiol* 2001, 74, 760–764. [PubMed: 11783930]
- (39). Kessel D; Luo Y Intracellular Sites of Photodamage as a Factor in Apoptotic Cell Death. *J. Porphyrins Phthalocyanines* 2001, 5, 181–184.
- (40). Reiners JJ Jr.; Caruso JA; Mathieu P; Chelladurai B; Yin X-M; Kessel D Release of Cytochrome C and Activation of ProCaspase-9 Following Lysosomal Photodamage Involves Bid Cleavage. *Cell Death Differ* 2002, 9, 934–944. [PubMed: 12181744]
- (41). Wang X The Expanding Role of Mitochondria in Apoptosis. *Genes Dev* 2001, 15, 2922–2933. [PubMed: 11711427]
- (42). Wang Y; Tjandra N Structural Insights of tBid, the Caspase-8-Activated Bid, and its BH3 Domain. *J. Biol. Chem* 2013, 288, 35840–35851. [PubMed: 24158446]

- (43). Epand RF; Martinou J-C; Fornallaz-Mulhauser M; Hughes DW; Epand RM The Apoptotic Protein tBid Promotes Leakage by Altering Membrane Curvature. *J. Biol. Chem* 2002, *277*, 32632–32639. [PubMed: 12082098]
- (44). Grinberg M; Sarig R; Zaltsman Y; Frumkin D; Grammatikakis N; Reuveny E; Gross A tBID Homooligomerizes in the Mitochondrial Membrane to Induce Apoptosis. *J. Biol. Chem* 2002, *277*, 12237–12245. [PubMed: 11805084]
- (45). Lovell JF; Billen LP; Bindner S; Shamas-Din A; Fradin C; Leber B; Andrews DW Membrane Binding by tBid Initiates an Ordered Series of Events Culminating in Membrane Permeabilization by Bax. *Cell* 2008, *135*, 1074–1084. [PubMed: 19062087]
- (46). Ott M; Norberg E; Zhivotovsky B; Orrenius S Mitochondrial Targeting of tBid/Bax: A Role for the TOM Complex? *Cell Death Differ* 2009, *16*, 1075–1082. [PubMed: 19521421]
- (47). Bogner C; Leber B; Andrews DW Apoptosis: Embedded in Membranes. *Curr. Opin. Cell Biol* 2010, *22*, 845–851. [PubMed: 20801011]
- (48). Kim H; Tu H-C; Ren D; Takeuchi O; Jeffers JR; Zambetti GP; Hsieh JJ-D; Cheng EH-Y Stepwise Activation of BAX and BAK by tBID, BIM, and PUMA Initiates Mitochondrial Apoptosis. *Mol. Cell* 2009, *36*, 487–499. [PubMed: 19917256]
- (49). Ai X; Mu J; Xing B Recent Advances of Light-Mediated Theranostics. *Theranostics* 2016, *6*, 2439–2457. [PubMed: 27877246]
- (50). Hyemin K; Beack S; Han S; Myeonghwan S; Lee T; Park Y; Kim KS; Yetisen AK; Yun SH; Kwon W; Hahn SK Multifunctional Photonic Nanomaterials for Diagnostic, Therapeutic, and Theranostic Applications. *Adv. Mater* 2018, *30*, 1701460 (pp 30).
- (51). Jiang X-M; Wang L-M; Wang J; Chen C-Y Gold Nanomaterials: Preparation, Chemical Modification, Biomedical Applications and Potential Risk Assessment. *Appl. Biochem. Biotechnol* 2012, *166*, 1533–1551. [PubMed: 22278050]
- (52). Liu Y; Zhao Y; Sun B; Chen C Understanding the Toxicity of Carbon Nanotubes. *Acc. Chem. Res* 2013, *46*, 702–713. [PubMed: 22999420]
- (53). Oldenborg P-A; Zheleznyak A; Fang Y-F; Lagenaur CF; Gresham HD; Lindberg FP Role of CD47 as a Marker of Self on Red Blood Cells. *Science* 2000, *288*, 2051–2054. [PubMed: 10856220]
- (54). Hwang Y; Yoon H; Choe K; Ahn J; Jung JH; Park J-H; Kim P In Vivo Cellular-Level Real-Time Pharmacokinetic Imaging of Free-Form and Liposomal Indocyanine Green in Liver. *Biomed. Opt. Express* 2017, *8*, 4706–4716. [PubMed: 29082096]
- (55). Ren H; Liu J; Li Y; Wang H; Ge S; Yuan A; Hu Y; Wu J Oxygen Self-Enriched Nanoparticles Functionalized with Erythrocyte Membranes for Long Circulation and Enhanced Phototherapy. *Acta Biomater* 2017, *59*, 269–282. [PubMed: 28663143]
- (56). Spiller W; Kliesch H; Wöhrle D; Hackbarth S; Röder B; Schnurpfeil G Singlet Oxygen Quantum Yields of Different Photosensitizers in Polar Solvents and Micellar Solutions. *J. Porphyrins Phthalocyanines* 1998, *2*, 145–158.
- (57). Costes SV; Daelemans D; Cho EH; Dobbin Z; Pavlakis G; Lockett S Automatic and Quantitative Measurement of Protein-Protein Colocalization in Live Cells. *Biophys. J* 2004, *86*, 3993–4003. [PubMed: 15189895]
- (58). Kalyanaraman B; Darley-USmar V; Davies K; Dennery P; Forman H; Grisham M; Mann G; Moore K; Roberts L II; Ischiropoulos H Measuring Reactive Oxygen and Nitrogen Species with Fluorescent Probes: Challenges and Limitations. *Free Radical Biol. Med* 2012, *52*, 1–6. [PubMed: 22027063]
- (59). Yu Z; Sun Q; Pan W; Li N; Tang B A Near-Infrared Triggered Nanophotosensitizer Inducing Domino Effect on Mitochondrial Reactive Oxygen Species Burst for Cancer Therapy. *ACS Nano* 2015, *9*, 11064–11074. [PubMed: 26456218]
- (60). Nam G; Rangasamy S; Ju H; Samson AAS; Song JM Cell Death Mechanistic Study of Photodynamic Therapy Against Breast Cancer Cells Utilizing Liposomal Delivery of 5,10,15,20-tetrakis(benzo[b]thiophene) *Porphyrin*. *J. Photochem. Photobiol., B* 2017, *166*, 116–125. [PubMed: 27889618]

- (61). Rizvi I; Anbil S; Alagic N; Celli JP; Zheng LZ; Palanisami A; Glidden MD; Pogue BW; Hasan T
PDT Dose Parameters Impact Tumoricidal Durability and Cell Death Pathways in a 3D Ovarian
Cancer Model. *Photochem. Photobiol* 2013, 89, 942–952. [PubMed: 23442192]

Author Manuscript

Author Manuscript

Author Manuscript

Author Manuscript

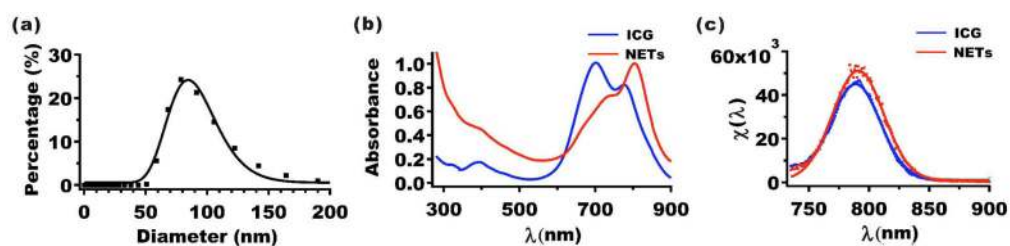


Figure 1.

Characterization of NETs. (a) Hydrodynamic diameter distribution of NETs as determined by DLS. Squares and error bars (too small to be seen) represent the mean and standard deviations of diameters, respectively ($n = 4$ measurements). The estimated mean diameter as determined from the log-normal fits (solid curves) is ≈ 85 nm. (b) Absorption spectra of $13 \mu\text{M}$ free ICG and NETs ($[\text{ICG}_{\text{NETs}}] \approx 10 \mu\text{M}$). (c) Normalized fluorescence emission spectra ($\chi(\lambda)$) (see eq 1) (squares) and Gaussian fits (solid curves) of $4 \mu\text{M}$ free ICG and NETs ($[\text{ICG}_{\text{NETs}}] \approx 2 \mu\text{M}$) in response to photoexcitation at 720 ± 2.5 nm. Solvent used in spectral recordings was 310 mOsm PBS.

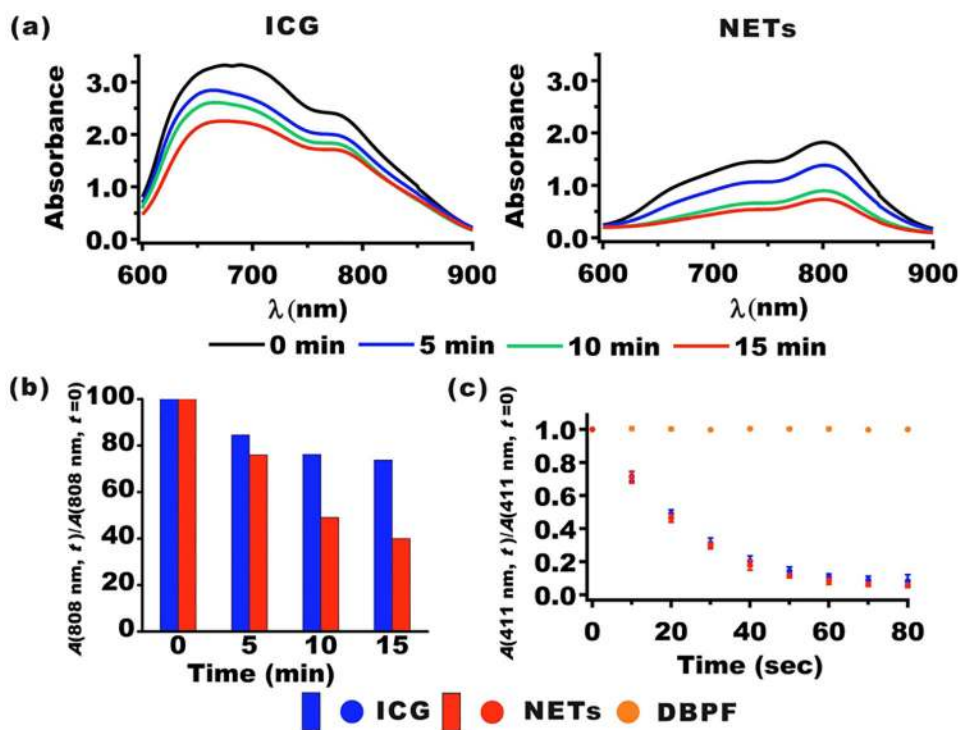


Figure 2. Photostability and $^1\text{O}_2$ generation of NETs in solution. (a) Absorption spectra of 22 μM free ICG and NETs ($[\text{ICG}_{\text{NETs}}] \approx 18 \mu\text{M}$) before and after 808 nm laser irradiation ($I_0 = 680 \text{ mW/cm}^2$) for 5, 10, and 15 min. (b) Normalized 808 nm absorbance values for ICG and NETs as a function of 808 nm laser irradiation time. (c) Normalized 411 nm absorbance values for solutions containing 10 μM DPBF without or with 11 μM ICG or NETs ($[\text{ICG}_{\text{NETs}}] \approx 18 \mu\text{M}$) as a function of 808 nm laser irradiation time. Data points and error bars in panel (c) represent the mean and SDs for $n = 4$ samples.

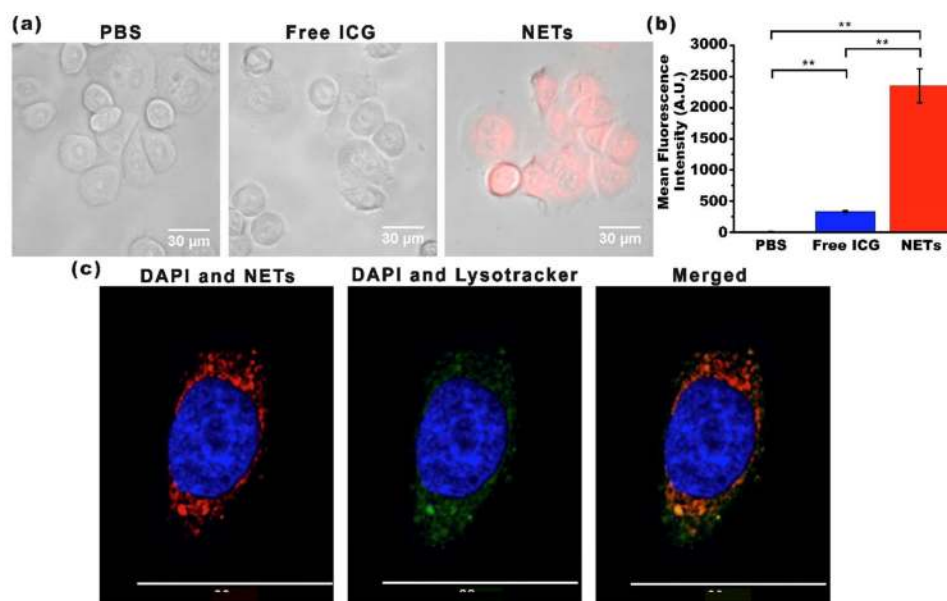


Figure 3. Uptake of NETs by SKBR3 cancer cells. (a) Merged bright-field and fluorescent images of SKBR3 cancer cells following 3 h of incubation at 37°C with PBS, 44 μM free ICG, or NETs ($[ICG_{NETs}] \approx 36 \mu M$). Images are falsely colored. Red channel: NIR emission due to ICG from NETs; gray channel: bright-field. (b) Uptake analysis of SKBR3 cells by flow cytometry. Geometric mean fluorescence intensity ($n = 3$ different samples) $**p < 0.01$. (c) Laser scanning confocal fluorescent images of a SKBR3 cell following 3 h of incubation at 37°C with NETs. Images are falsely colored. Blue channel: DAPI; green channel: Lysotracker; red channel: NIR emission due to ICG from NETs.

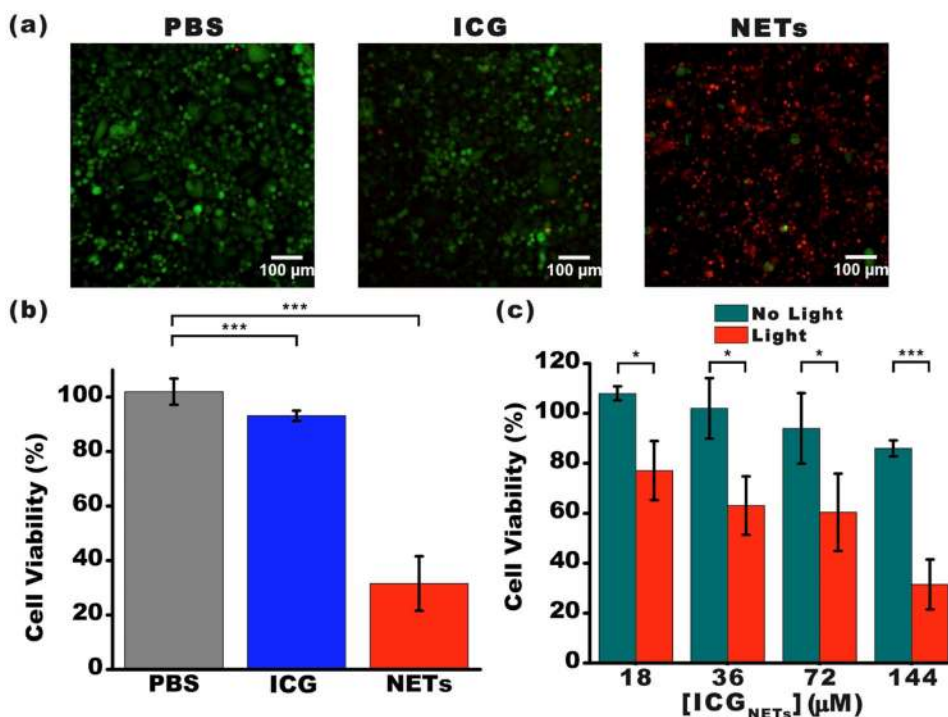


Figure 4. Photodestruction of SKBR3 cancer cells in vitro. (a) Fluorescent images of SKBR3 cancer cells incubated with PBS (negative control), 176 μM free ICG (positive control), and NETs ($[ICG_{NETs}] \approx 144 \mu M$) for 3 h at 37°C and followed by 808 nm laser irradiation at $I_0 = 680 \text{ mW/cm}^2$ for 15 min. Live cells were identified by the Calcein AM stain and falsely colored in green. Dead cells in response to laser irradiation were identified using the EthD-1 stain and falsely colored in red. (b) Percentage viability of SKBR3 cells as a function of incubation agent. (c) Percentage viability of SKBR3 cells as a function of $[ICG_{NETs}]$. In panels (b) and (c), statistically significant differences are indicated as * $p < 0.05$ and *** $p < 0.001$ ($n = 3$ samples for each treatment).

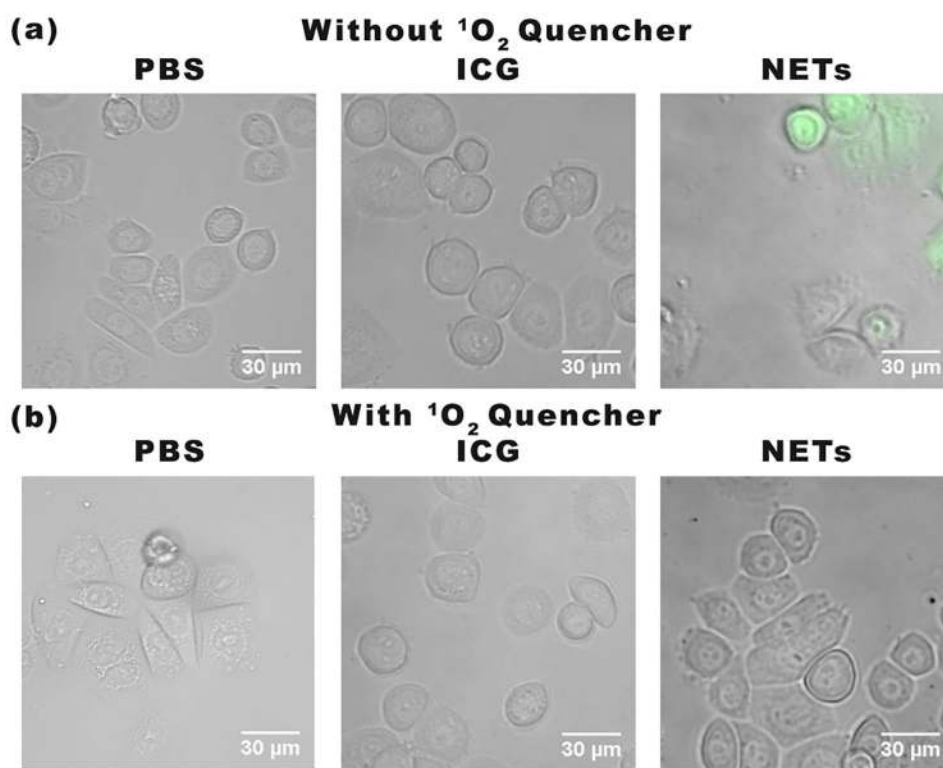


Figure 5. Detection of ROS generation by cell imaging. We present merged bright-field and DCF fluorescence images of SKBR3 cancer cells incubated with PBS, 44 μM free ICG, or NETs ([ICGNETs] \approx 36 μM) for 3 h and subsequently irradiated at 808 nm for 15 min at $I_0 = 680 \text{ mW/cm}^2$. Images correspond to (a) without and (b) with application of $^1\text{O}_2$ quencher, sodium azide. Images are falsely colored. Gray channel: bright-field. Green channel: fluorescence emission from DCF.

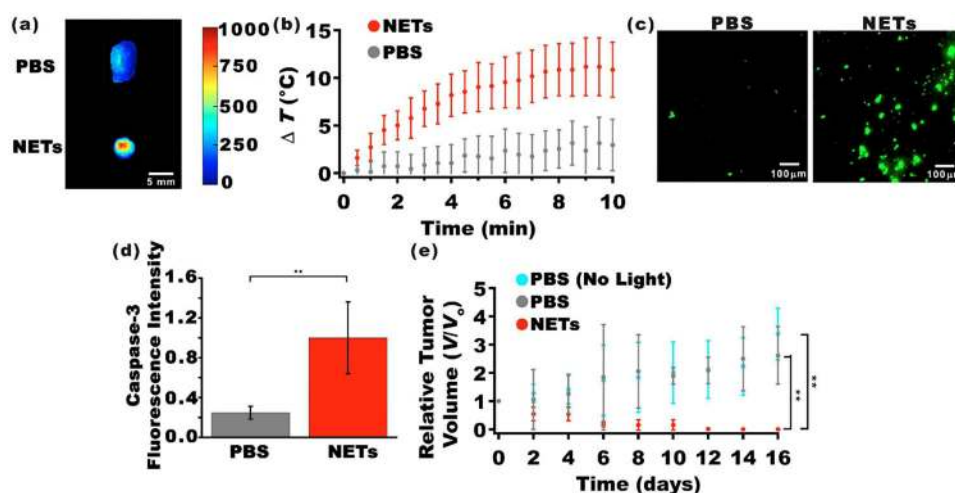


Figure 6.

NIR fluorescence imaging and photodestruction of xenograft tumors in mice. (a) NIR fluorescence images of tumors extracted 24 h after tail injection of PBS (top panel) and NETs ($[ICG_{NETs}] \approx 980 \mu M$) (bottom panel). Scale bar on the right corresponds to fluorescent intensity (photoexcitation at 700 ± 30 nm and emission >810 nm collected). (b) Temperature rise as a function of laser irradiation time as measured by a thermocouple needle probe placed ≈ 1 mm below the skin surface and ≈ 2 mm outside the irradiated spot. (c) Fluorescent images of sectioned tumors by immunostaining using FITC-labeled Caspase-3 antibody. (d) Fluorescence emission intensity associated with FITC-labeled Caspase-3 antibody as the apoptosis indicator following laser irradiation. (e) Estimated relative change in tumor volumes (V) of nonorthotopic xenograft tumors in mice with respect to the volumes at time zero (V_0). Time zero is with respect to the day of laser irradiation. Mice were injected via the tail vein with 100 μL of either PBS or NETs ($[ICG_{NETs}] \approx 980 \mu M$). Laser irradiation was done 24 h postinjection of NETs or PBS. Irradiation parameters were as follows: 808 nm; spot size = 9 mm; irradiation time = 10 min; $I_0 = 680$ mW/cm². In panels (b) and (e), $n = 4$ mice for each administered agent. In panel (d), $n = 5$ images from different sections of the same tumor for each administered agent (statistically significant difference at $**p < 0.01$).